

# Experimental Demonstration of A Dual-Input/Dual-Output Reflective Impedance Metasurface

Jean Louis Keyrouz, Vasileios G. Ataloglou, George V. Eleftheriades

**Abstract**—This paper presents the experimental demonstration of a dual-input/dual-output reflective impedance metasurface. The design of the metasurface relies on the Method of Moments and leverages auxiliary surface waves to achieve anomalous reflection of impinging plane waves with controlled sidelobe levels. A prototype that ensures maximum directivity at prescribed angles for the reflection of the two input waves is then fabricated on a Rogers RO3003 printed-circuit board using 42 metawires loaded with printed capacitors. The proposed metasurface is capable of reflecting incident beams from  $-20^\circ$  to  $0^\circ$  and from  $+20^\circ$  to  $-40^\circ$  at 9.7 GHz. The metasurface is measured and an aperture efficiency of at least 80% is calculated for each of the reflected waves, indicating a high multiplexing efficacy.

**Index Terms**—Metasurfaces, multiple-inputs, beamforming, impedance-layer optimization.

## I. INTRODUCTION

THE advent of new wireless communication systems has elicited a renewed interest in the development of energy efficient and compact beamforming antennas using metasurfaces (MTSs). In fact, MTSs have been used in a wide range of applications showcasing their exceptional ability to mold electromagnetic waves in various ways, such as perfect anomalous refraction [1], [2], perfect anomalous reflection [3], [4], beamforming [5], [6], and polarization control [7], [8].

Metasurfaces have also facilitated the design of structures that radiate multiple independent beams, when fed by multiple spatially-separated feed points. Each feed point produces a beam in a different direction, enabling multiple-input multiple-output (MIMO) communications with the use of a single aperture. In the context of holographic antennas, the design with multiple feeds and multiple output beams is typically done by averaging the impedance of all the different cases [9]–[11]. The same method of multiplexing has also been proposed in the case that the feeds operate in different frequencies [12], [13]. While the averaging multiplexing method provides some enhancement in the aperture efficiency of all beams compared to partitioning the metasurface into different regions, it still suffers from cross interference-terms, namely the radiation that is produced when the wave from each feed interacts with the modulation designed for the other feeds. Therefore, unless there is orthogonality of the incident fields/modulations or the position of the feeds is carefully optimized, the total performance would be sub-optimal. A solution was proposed in [14] by forming an over-defined stacked system of equations for the unknown impedances based on integral equations and

the desired radiated fields. This is solved in a quasi-direct approach using the least square method [15].

On the other hand, integral equation models solved using the Method of Moments and using a classic iterative optimization approach for determining the necessary impedances for desired functionalities have been recently proposed [16], [17]. While these methods directly optimize for the far-field pattern, the underlying mechanism is the excitation of auxiliary surface waves that redistribute the power passively along the MTS [18]–[20]. In addition to capturing the mutual coupling interactions between the different unit cells comprising the MTS, integral equation methods enable the realization of MIMO scenarios. The iterative optimization approach have certain benefits as the exact solution for all inputs is available at each iteration during optimization. In the case of multiple incident fields, this means that the optimization scheme treats all cases rigorously, and there are not any unpredicted cross-interference terms. Moreover, constraints can be set in the the range of impedance values so that the latter are physically realizable. Lastly, a set of metrics such as the directivity or the sidelobe level can be introduced in the cost function to balance the requirements of each application. Using this approach, a multi-layered structure has been proposed of shaping the reflected radiation pattern for two different frequencies [21].

In this paper, we discuss the design and measurement of a MIMO single-layer reflective impedance MTS that anomalously reflects two plane waves in an asymmetric manner. Such a reflective passive MTS can be used to redirect beams in an indoor wireless environment. The efficient anomalous reflection of two incident beams effectively doubles the number of channels that the MTS can handle simultaneously. The metasurface is designed based on the integral-equation optimization framework presented in [17] to maximize the directivity of two reflected plane waves at predetermined angles, while keeping the sidelobes at a tolerable level. The anomalous reflection of the plane waves is made possible through the passive excitation of auxiliary surface waves. The proposed design is fabricated on a Rogers RO3003 printed-circuit-board with sub-wavelength printed capacitor unit cells etched on its surface resulting in a compact and lightweight structure. Finally, the far-field reflections of two impinging planes waves are measured in a bi-static setup at 9.7 GHz.

The rest of the paper is organized as follows. Section II details the geometry of the MTS, the optimization algorithm used to generate the metawire loadings and the characterization of printed capacitor unit cells to implement the metawires.

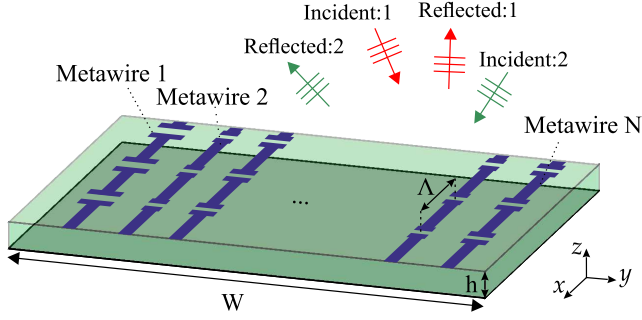


Fig. 1. Model of the impedance MTS with printed capacitor unit cells.

Section III outlines the design, fabrication and measurement of a reflective impedance MTS that anomalously reflects two plane waves. Finally, the paper is concluded in Sec. IV.

## II. THEORETICAL MODEL

The designed structure consists of a set of metawires on top of a grounded dielectric substrate of thickness  $h$  and relative permittivity  $\epsilon_r$ . The substrate has a width of  $W$  along the  $y$  direction while the metawires are assumed to be infinite along the  $x$  direction with periodic capacitive loadings every  $\Lambda$ . The very sub-wavelength nature of the periodic loadings allows us to assign a homogenized loading impedance  $Z_i$  at every metawire ( $i$ ). The different impedance loadings  $Z_i$  are implemented using printed capacitors of varying lengths, as shown in Fig. 1.

The MTS is illuminated with transverse electric (TE) plane waves ( $\mathbf{E}_{\text{inc}}^n = E_{\text{inc}}^n \hat{\mathbf{x}}$ ) at specific incident angles  $\theta_{in}$  in the  $yz$  plane, with  $n$  representing the different inputs. Each incident field  $E_{\text{inc}}^n$  induces surface conduction currents  $J_g$  and  $J_w$  in the ground plane and the metawires respectively, as well as, volume polarization currents  $J_v$  in the dielectric. The scattered fields generated by these three induced currents, in addition to the incident field, form the total field radiated by the MTS. A set of coupled equations for  $J_g, J_v$  and  $J_w$  is formed by inspecting the total electric field at the different regions. The total electric field must be zero on the ground plane because it is entirely tangential to it. According to Ohm's law, the total electric field is proportional to  $J_w$  with a proportionality constant of  $Z_i$  at every metawire ( $i$ ) and proportional to  $J_v$  in the dielectric substrate. Expanding the unknown conduction and polarization currents using the MoM into pulse basis functions and using point matching at the center of each basis function leads to the following linear system of equations [17]:

$$\left( \begin{bmatrix} 0 & 0 & 0 \\ 0 & P & 0 \\ 0 & 0 & Z_w \end{bmatrix} - \begin{bmatrix} G_{gg} & G_{gv} & G_{gw} \\ G_{vg} & G_{vv} & G_{vw} \\ G_{wg} & G_{wv} & G_{ww} \end{bmatrix} \right) \begin{bmatrix} \bar{J}_g \\ \bar{J}_v \\ \bar{J}_w \end{bmatrix} = \begin{bmatrix} \bar{E}_i^g \\ \bar{E}_i^v \\ \bar{E}_i^w \end{bmatrix}, \quad (1)$$

where  $P$  and  $Z_w$  are diagonal matrices related to the electric susceptibility of the substrate and the loading impedances metawires  $Z_i$  respectively, the  $\bar{J}$  entries represent the sampled induced currents, the  $G$  entries represent the self and mutual interactions between the various components of the impedance MTS and the  $\bar{E}_i$  entries represent each incident field sampled

at the ground plane, substrate and metawires. The derived induced currents are then used to determine the different scattered fields radiated from the MTS in the far-field. A more detailed description of the integral equation framework used in our analysis can be found in [17].

The impedance loadings  $Z_i$  can be optimized to achieve the desired radiation pattern for any given incident field  $E_{\text{inc}}^n$ , since Eq. (1) is valid for any illumination of the MTS. Naturally, different incident fields in Eq. (1) would result in different set of induced currents and, thus, different far-field patterns for each input. In fact, if we consider a dual-input/dual-output system ( $n=1,2$ ), the goal is to optimize for a single set of impedances  $Z_i$  that will allow each incident electric field to induce the necessary currents to achieve the desired far-field radiation patterns  $D_n^{ff}$ .

In this work, we primarily aim to achieve maximum directivity at the desired output angles  $\theta_{on}$ , while maintaining a satisfactory sidelobe level. The cost function that quantifies these features for two incident angles ( $n=1,2$ ) can be defined as follows:

$$F = - \sum_{n=1}^2 D_n^{ff}(\theta_{on}) + \sum_{n=1}^2 \max\{D_n^{ff}(\theta_{on}^{\text{SLL}}) - S_n, 0\}, \quad (2)$$

where  $D_n^{ff}(\theta_{on})$  represents the directivity at the desired output angles  $\theta_{on}$ ,  $D_n^{ff}(\theta_{on}^{\text{SLL}})$  represents the directivity at a set of angles  $\theta_{on}^{\text{SLL}}$  that excludes the main beam, and  $S_n$  represents the maximum level the sidelobes can reach, all in dB scale. The first term guarantees maximal directivity in the chosen directions  $\theta_{on}$  while the second term prevents any sidelobe defined in the set of angles  $\theta_{on}^{\text{SLL}}$  from rising above a predetermined absolute level  $S_n$ . Minimization of the cost function is done in MATLAB using the built-in genetic algorithm followed by gradient descent optimization. The output of the genetic algorithm is inherently random so multiple iterations of the optimization algorithm can be performed before selecting the solution with the optimal pattern. Due to the physical limitations when realizing the sub-wavelength unit cells, a constraint is placed beforehand on the range of values for the imaginary part of the impedance loadings  $\text{Im}\{Z_i\}$ .

For the presented example, only capacitive loadings are utilized, since the achievable range is sufficient to realize the desired functionality. A correspondence between the capacitive loading  $Z_{\text{load}}$  and a printed capacitor is established by characterizing a single capacitive unit cell in Ansys High-Frequency Structure Simulator (HFSS). In fact, an embedded source is placed below the unit cell and a full-wave simulation is then performed to record the electric fields emanating from the structure for different capacitor lengths. A similar procedure is performed with a homogenized strip of varying impedance  $Z_{\text{load}}$  using the MoM framework presented in this Section. A comparison of these two fields links the different capacitor lengths to a complex impedance  $Z_{\text{load}}$ , as shown in Fig. 2. Using the above-described procedure to characterize a single metawire avoids placing it in an infinite periodic array, typically found in metasurface or reflectarray designs. This is aligned with the MoM optimization framework which models the homogenized impedance loading of a single metawire and

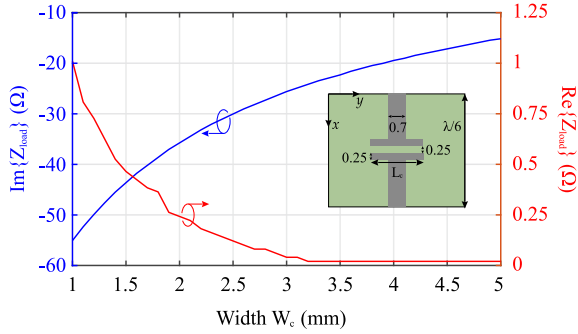


Fig. 2. Impedance loading variation  $Z_{1\text{load}}$  as a function of the length of a printed capacitor.

includes all mutual coupling interactions between dissimilar neighboring metawires.

### III. DUAL-INPUT DUAL-OUTPUT REFLECTIVE IMPEDANCE METASURFACE

In this section, we outline the design and measurement of a reflective impedance MTS that displays the anomalous reflection of two incident plane waves at desired angles. The designed MTS consists of 42 metawires with a loading period of  $\Lambda = \lambda/6$  on top of a grounded substrate of height  $h = 1.52$  mm, permittivity  $\epsilon_r = 3$  and loss tangent  $\tan(\delta) = 0.001$ . It has a width of  $W = 8\lambda$  at 10 GHz. The MTS reflects two incident beams  $20^\circ$  off their specular direction. In fact, two uniform plane waves impinging on the surface at  $\theta_{i1} = -20^\circ$  and  $\theta_{i2} = +20^\circ$  are anomalously reflected at  $\theta_{o1} = 0^\circ$  and  $\theta_{o2} = -40^\circ$  respectively.

The optimization algorithm previously discussed was run multiple times to obtain a pattern with a sufficiently low cost function value. The sidelobe level parameters in Eq.(2)  $S_1$  and  $S_2$  were set in a way that ensures a sidelobe level at most equal to  $-13.3$  dB when measured from the peak. The optimization is performed on the imaginary parts of the loading impedances  $\text{Im}\{Z_i\}$ , as the effect of the real parts  $\text{Re}\{Z_i\}$  on the radiation pattern is minimal. The range of  $\text{Im}\{Z_i\}$  was constrained to  $[-55, -15]\Omega$  and the optimized loading impedances  $Z_i$  are shown in Fig 3. The length of the MTS in the wire longitudinal direction (x-axis) was truncated to around  $6\lambda$ . Using finite-length homogenized impedance sheets, full-wave simulations in HFSS showed that such a truncation is sufficient to approximate the assumed uniformity along the x-axis and maintain an acceptable far-field pattern. The design was implemented on a 21.8 cm by 23.98 cm board using a Rogers RO3003 substrate with the metawires etched on one side while the other side is kept copper laminated to serve as a ground plane.

The antenna is measured in a far-field anechoic chamber with two identical X-band horn antennas acting as the transmitter and receiver, as shown in Fig. 4. The measuring antennas are around 156 cm away from the MTS to ensure that the receiving antenna is in the far-field region. This distance is sufficient to approximate the waves emitted by the horn antenna with plane waves at the location of the MTS. The transmitting horn antenna is fixed to the ground while

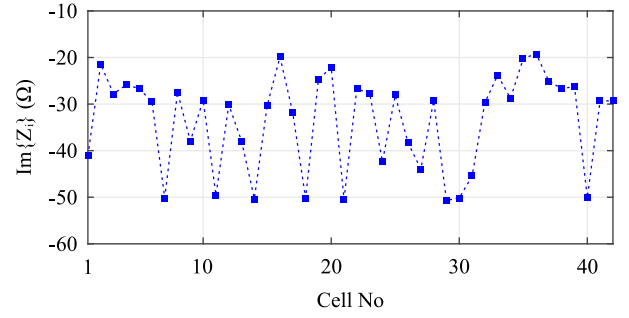


Fig. 3. Optimized set of loading impedances  $\text{Im}\{Z_i\}$  for the 42 metawires.

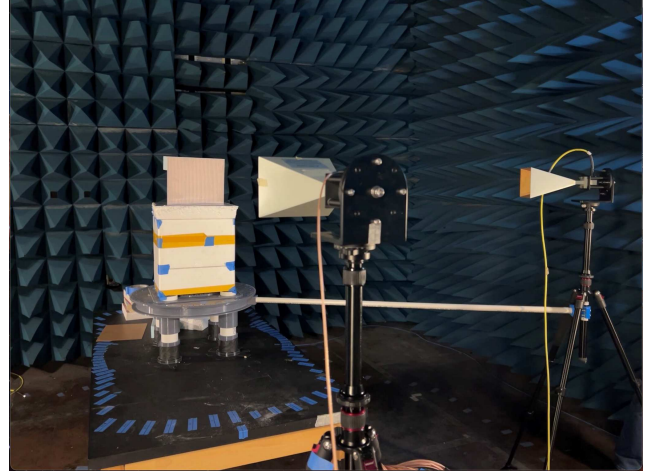


Fig. 4. Bi-static measurement setup. The transmitting antenna illuminates the MTS with a plane wave, while the rotating receiving antenna records the reflected far-field pattern.

the MTS is rotated by  $20^\circ$  in both directions to emulate an incidence at  $\pm 20^\circ$ . Both the receiving and transmitting horn antennas are mounted on tripods connected by plastic tubes to the platform on which the MTS is placed. This ensures the receiving antenna is maintaining a constant distance from the MTS when measurements are taken at the different angles. The MTS suffers from a slight warping due to fabrication so it has been clipped to a rigid board to mitigate the bending. The clips are practically invisible to the incident radiation and do not affect the performance of the MTS. Measurements of  $S_{21}$  are performed with a resolution of  $1^\circ$  near the main beam and up to  $5^\circ$  near the sidelobes. The horn antennas occupy a region of around  $7.5^\circ$  each, which prohibits measurements of the reflected beam in a  $15^\circ$  region around the incident angle.

A copper plate with dimensions similar to the MTS is used to scale the measurement results. To be more specific, the difference between the measured and theoretical specular reflection from the copper plate is added to all measured values. The measurement results are shown in Fig. 5 alongside the HFSS radiation pattern simulation, both at 9.7 GHz. The measured gain pattern is similar to the pattern simulated on HFSS. The specular direction gain is heavily suppressed demonstrating the efficacy of the MTS in reflecting the input beams at the desired directions. The maximum gain of the first measured pattern occurs at  $\theta_{o1} = -1^\circ$  with a gain of 15.8 dB

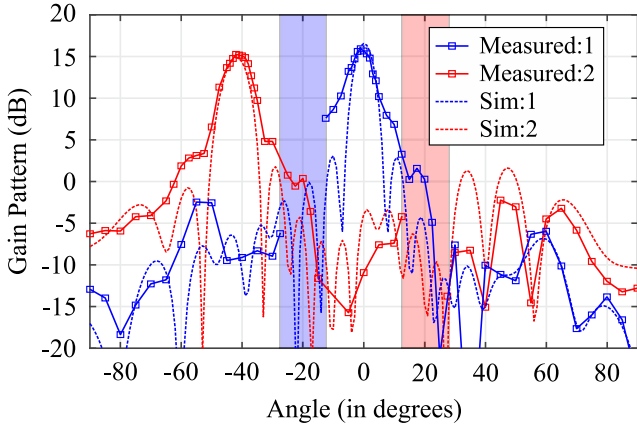


Fig. 5. Gain radiation patterns of the measurements and HFSS full wave simulations at 9.7 GHz. The shaded areas represent the zones where no measurements are possible ( $[-27.5^\circ, -12.5^\circ]$  for the first incident beam and  $[12.5^\circ, 27.5^\circ]$  for the second incident beam).

which is around 1 dB lower compared to the maximum gain of the HFSS design of 16.8 dB. Moreover, the maximum gain of the second measured pattern occurs at  $\theta_{o2} = -41^\circ$  with a gain of 15.0 dB, which is around 0.2 dB lower compared to the maximum gain of the HFSS design of 15.2 dB. Full-wave simulations of the design with a cylindrical source  $50\lambda$  away (similar to the measurement setup) showed a drop in the maximum directivity and a slight broadening of the beam when compared to the plane wave incidence. Those effects were more pronounced in the first case (0.45 dB drop) than in the second case (0.2 dB drop). We note that although the design was optimized for 10 GHz, a shift was observed in experiments for the operating frequency from 10 GHz to around 9.7 GHz which is attributed to a shift in the permittivity of the substrate. This is why the presented simulation results in Fig. 6 are also at 9.7 GHz with an assumed dielectric constant of  $\epsilon_r = 3.25$ . In fact, HFSS simulations of the same MTS design on a substrate of  $\epsilon_r = 3.25$  at 9.7 GHz match quite well the bandwidth patterns of the measured waves, as shown in Fig. 6. The 3-dB bandwidth is 8.4% and 8.1% for the measured and simulated pattern directed at  $0^\circ$ , respectively. Similarly, the 3-dB bandwidth is 6.8% and 7.4% for the measured and simulated pattern directed at  $40^\circ$ , respectively. We can clearly see that there has been a shift from the original design with  $\epsilon_r = 3$  at 10 GHz to  $\epsilon_r = 3.25$  at 9.7 GHz.

We calculate the ideal 2D directivity of an aperture with uniform-amplitude based on [22]:

$$D_{uni}^{ff}(\theta_{on}) = \frac{2\pi W}{\lambda} \cos(\theta_{on}). \quad (3)$$

The illumination and power efficiencies, which are defined as:

$$\eta_{il} = \frac{\max(D^{ff}(\theta))}{D_{uni}^{ff}(\theta_{on})} \quad \eta_p = \frac{P_{ref}}{P_{inc}} \quad (4)$$

are used to calculate the total aperture efficiency of the HFSS radiation pattern where  $D(\theta)$  represents the directivity pattern,  $P_{ref}$  the reflected power and  $P_{inc}$  the incident power. For the wave incident at  $\theta_{i1} = -20^\circ$  and reflected at  $\theta_{o1} = 0^\circ$ ,

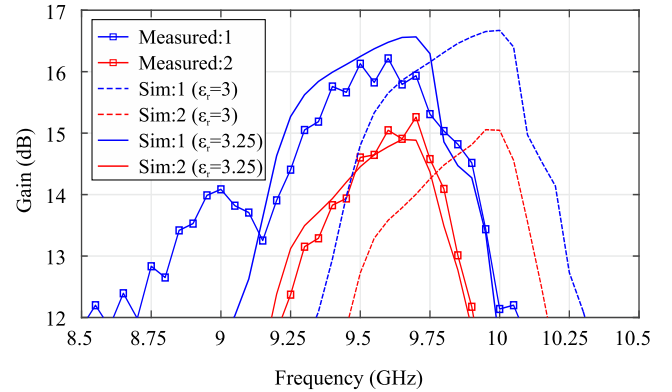


Fig. 6. Bandwidth plots of the measured and simulated design. The plots at 10 GHz were measured at  $+1^\circ$  and  $-41^\circ$  while the plots at 9.7 GHz were measured at  $0^\circ$  and  $-42^\circ$ .

$\eta_{il} = 0.993$  and  $\eta_p = 0.936$  therefore the total aperture efficiency is  $\eta = \eta_{il}\eta_p = 93.0\%$ . Similarly, for the wave incident at  $\theta_{i2} = +20^\circ$  and reflected at  $\theta_{o2} = -40^\circ$ ,  $\eta_{il} = 0.897$  and  $\eta_p = 0.918$  therefore the total aperture efficiency is  $\eta = \eta_{il}\eta_p = 82.5\%$ . On the other hand, the aperture efficiency of the measured wave at  $\theta_{o1} = 0^\circ$  is equal to  $\eta = 80.3\%$  and at  $\theta_{o2} = -40^\circ$  is equal to  $\eta = 89.9\%$ . There is an efficiency drop in the first case mostly due to the slight broadening of the main beam. This is attributed to both the mild warping in the fabricated design and the slightly nonuniform illumination of the MTS. The deficiencies present in the current MTS can be fixed in future designs by employing more rigid substrates in the fabrication of the MTS.

#### IV. CONCLUSION

In conclusion, we presented an experimental demonstration of a reflective impedance metasurface that handles two incident beams simultaneously. The uniform plane waves impinging on the surface at  $\pm 20^\circ$  are anomalously reflected at  $-40^\circ$  and  $0^\circ$  at 9.7 GHz, respectively, while keeping the sidelobe level at a reasonable level. The metasurface was designed using a Method of Moments based optimization framework. The physical design was fabricated and measured for both input channels reporting highly directive beams in the desired directions, as evident from the radiation pattern and the high aperture efficiencies.

#### REFERENCES

- [1] M. Selvanayagam and G. V. Eleftheriades, "Discontinuous electromagnetic fields using orthogonal electric and magnetic currents for wavefront manipulation," *Opt. Exp.*, vol. 21, issue 12, pp. 14 409-14 429, Jun 2013.
- [2] C. Pfeiffer and A. Grbic, "Metamaterial Huygens' surfaces: Tailoring wave fronts with reflectionless sheets," *Phys. Rev. X*, vol. 110, no. 19, pp. 197401-197401, 2013.
- [3] A. M. H. Wong and G. V. Eleftheriades, "Perfect Anomalous Reflection with a Bipartite Huygens' Metasurface," *Phys. Rev. X*, vol. 8, no. 1, pp. 011036-011036, 2018.
- [4] H. Chalabi, Y. Ra'adi, D. L. Sounas, and A. Alù, "Efficient anomalous reflection through near-field interactions in metasurfaces," *Phys. Rev. B*, vol. 96, no. 7, 2017.
- [5] A. H. Dorrah and G. V. Eleftheriades, "Bianisotropic Huygens' metasurface pairs for non-local power-conserving wave transformations," *IEEE Antennas Wireless Propag. Lett.*, vol. 17, no. 10, pp. 1788-1792, 2018.

- [6] B. O. Raeker and A. Grbic, "Compound Metaoptics for Amplitude and Phase Control of Wave Fronts," *Phys. Rev. Lett.*, vol. 122, no. 11, pp. 113901–113901, 2019.
- [7] M. Selvanayagam and G. V. Eleftheriades, "Polarization Control Using Tensor Huygens Surfaces," *IEEE Trans. Antennas Propag.*, vol. 62, no. 12, pp. 6155–6168, Dec. 2014.
- [8] T. Niemi, A. O. Karilainen and S. A. Tretyakov, "Synthesis of Polarization Transformers," *IEEE Trans. Antennas Propag.*, vol. 61, no. 6, pp. 3102–3111, Jun. 2013.
- [9] Y. B. Li, B. G. Cai, Q. Cheng, and T. J. Cui, "Isotropic Holographic Metasurfaces for Dual-Functional Radiations without Mutual Interferences," *Adv. Funct. Mater.*, vol. 26, no. 1, pp. 29–35, 2016.
- [10] D. González-Ovejero, G. Minatti, G. Chattopadhyay and S. Maci, "Multibeam by Metasurface Antennas," *IEEE Trans. Antennas Propag.*, vol. 65, no. 6, pp. 2923–2930, Jun. 2017.
- [11] A. V. Chesnitskiy, A. N. Kosmynin, O. M. Kaigorodov, P. A. Sibirtsev, K. N. Kosmynina and K. V. Lemberg, "Multibeam Antenna Implementation Using Anisotropic Metasurfaces," in *Proc. IEEE 23rd Int. Conf. Young Professionals Electron Devices Mater. (EDM)*, pp. 251–255, Jun. 2022.
- [12] Y. Li, A. Li, T. Cui and D. F. Sievenpiper, "Multiwavelength Multiplexing Hologram Designed Using Impedance Metasurfaces," *IEEE Trans. Antennas Propag.*, vol. 66, no. 11, pp. 6408–6413, Nov. 2018.
- [13] M. Faenzi, D. González-Ovejero, and S. Maci, "Overlapped and sequential metasurface modulations for Bi-Chromatic beams generation," *Appl. Phys. Lett.*, vol. 118, no. 18, pp. 181902–181902, 2021.
- [14] M. Bodehou, E. Martini, S. Maci, I. Huynen and C. Craeye, "Multi-beam and Beam Scanning With Modulated Metasurfaces," *IEEE Trans. Antennas Propag.*, vol. 68, no. 3, pp. 1273–1281, Mar. 2020.
- [15] M. Bodehou, C. Craeye, E. Martini and I. Huynen, "A Quasi-Direct Method for the Surface Impedance Design of Modulated Metasurface Antennas," *IEEE Trans. Antennas Propag.*, vol. 67, no. 1, pp. 24–36, Jan. 2019.
- [16] J. Budhu and A. Grbic, "Perfectly Reflecting Metasurface Reflectarrays: Mutual Coupling Modeling Between Unique Elements Through Homogenization," *IEEE Trans. Antennas Propag.*, vol. 69, no. 1, pp. 122–134, Jan. 2021.
- [17] G. Xu, V. G. Ataloglou, S. V. Hum, and G. V. Eleftheriades, "Extreme Beam-Forming With Impedance Metasurfaces Featuring Embedded Sources and Auxiliary Surface Wave Optimization", *IEEE Access*, vol. 10, pp. 28670–28684, Mar. 2022.
- [18] A. Epstein and G. V. Eleftheriades, "Synthesis of Passive Lossless Metasurfaces Using Auxiliary Fields for Reflectionless Beam Splitting and Perfect Reflection," *Phys. Rev. Lett.*, vol. 117, no. 25, pp. 256103–256103, 2016.
- [19] D.-H. Kwon and S. A. Tretyakov, "Arbitrary beam control using passive lossless metasurfaces enabled by orthogonally polarized custom surface waves," *Phys. Rev. B*, vol. 97, no. 3, 2018.
- [20] V. G. Ataloglou and G. V. Eleftheriades, "Arbitrary Wave Transformations With Huygens' Metasurfaces Through Surface-Wave Optimization," *IEEE Antennas Wireless Propag. Lett.*, vol. 20, no. 9, pp. 1750–1754, Sept. 2021.
- [21] J. Budhu, E. Michielssen and A. Grbic, "The Design of Dual Band Stacked Metasurfaces Using Integral Equations," *IEEE Trans. Antennas Propag.*, vol. 70, no. 6, pp. 4576–4588, Jun. 2022.
- [22] G. A. Egorov and G. V. Eleftheriades, "Theory and Simulation of Metasurface Lenses for Extending the Angular Scan Range of Phased Arrays," *IEEE Trans. Antennas Propag.*, vol. 68, no. 5, pp. 3705–3717, May 2020.